

Published in Nuclear Fusion as,
D.C. Pace, et al., Nucl. Fusion 51, 043012 (2011)
<http://dx.doi.org/10.1088/0029-5515/51/4/043012>

Transport of energetic ions due to sawteeth, Alfvén eigenmodes, and microturbulence

D.C. Pace¹ R.K. Fisher², M. García-Muñoz³, W.W. Heidbrink¹, G.R. McKee⁴, M. Murakami⁵, C.M. Muscatello¹, R. Nazikian⁶, J.M. Park⁵, C.C. Petty², T.L. Rhodes⁷, G.M. Staebler², M.A. Van Zeeland², R.E. Waltz², R.B. White⁶, J.H. Yu⁸, W. Zhang¹, and Y.B. Zhu¹

^{1,a} University of California-Irvine, Irvine, CA 92697, USA

² General Atomics, P.O. Box 85608, San Diego, CA 92186-5608

³ Max-Planck Institut für Plasmaphysik, Garching D-85748, Germany

⁴ University of Wisconsin-Madison, 1500 Engineering Dr., Madison, WI 53706, USA

⁵ Oak Ridge National Laboratory, PO Box 2008, Oak Ridge, TN 37831, USA

⁶ Princeton Plasma Physics Laboratory, PO Box 451, Princeton, NJ 08543-0451, USA

⁷ University of California-Los Angeles, PO Box 957099, Los Angeles, CA 90095, USA

⁸ University of California-San Diego, 9500 Gilman Dr., La Jolla, CA 92093, USA

E-mail: pacedc@fusion.gat.com

Abstract. Utilizing an array of new diagnostics and simulation/modeling techniques, recent DIII-D experiments have elucidated a variety of energetic ion transport behaviors in the presence of instabilities ranging from large-scale sawteeth to fine spatial scale microturbulence. Important new insights include: sawteeth, such as those of the ITER baseline scenario, cause major redistribution of the energetic ion population; high levels of transport induced by low-amplitude Alfvén eigenmodes can be caused by the integrated effect of a large number of simultaneous modes; and microturbulence can contribute to the removal of alpha ash while having little effect on fusion alphas. This paper provides an overview of recent and upcoming results from the DIII-D Energetic Particles research program.

PACS numbers: 52.55.Fa, 52.55.Pi, 52.35.Py, 52.35.Bj, 52.35.Ra

1. Introduction

Understanding and controlling the confinement of energetic ion populations in tokamaks is increasing in importance as we approach self-heated devices. In ITER, seemingly small reductions in fusion- α confinement can significantly reduce fusion power, and direct losses impacting the first-wall have the ability to cause damage [1, 2]. Collaborative work combining experimental and theoretical research is focused on the creation of accurate models for describing this resultant transport. Developing validated predictive models for the nonlinear interaction of energetic particles with plasma instabilities is vital for extrapolation to ITER and future devices since adequate confinement of the 3.5 MeV fusion born alpha particles is required in order to maintain a burning plasma state. Further, once these particles have deposited their energy, the challenge is to remove the resulting alpha ash before it contributes significant fuel dilution limiting the fusion rate at maximum beta.

DIII-D [3, 4] experiments employing a wide array of diagnostics have studied a variety of energetic ion transport processes. This paper provides an overview of recent and upcoming results from the Energetic Particles research program. Section 2 describes diagnostics that are particularly relevant to energetic ion studies. Section 3 presents results concerning the large spatial scale of sawtooth crash perturbations, which cause a redistribution of the energetic ion population that is measurable across the poloidal cross section [5]. Section 4 reports on the effects of intermediate scale Alfvénic instabilities [6, 7, 8] such as the toroidal Alfvén eigenmode (TAE) and the reversed shear Alfvén eigenmode (RSAE), where it is found that high levels of transport are capable of resulting from the integrated effect of a large number of simultaneous but low-amplitude modes [9, 10]. Section 5 concerns the fine spatial scale of microturbulence and it is shown that ion temperature gradient (ITG) and trapped electron mode (TEM) turbulence can contribute to the removal of alpha ash while having little to no effect on full energy fusion alpha particles [11, 12]. The conclusion given in Section 6 summarizes the present state of quantitative understanding with regard to these transport mechanisms.

2. Diagnostic Capability

The energetic ion population for these studies is generated by neutral beam injection (fast-wave injection is available but was not used in these cases). These neutral beams are capable of injection energies between 58 and 91 keV, thereby providing the ability to vary the energetic ion distribution. Figure 1 is a schematic diagram that indicates the positions and injection geometries of all eight neutral beams. Standard directions for the toroidal magnetic field (B_T) and plasma current (I_p) as shown in figure 1 were used for all of the experiments described here. In such a setup, the beam lines at toroidal angles of 30° , 150° , and 330° inject co-current ($v_{\parallel}/v > 0$) and the beams at 210° inject counter-current ($v_{\parallel}/v < 0$). The viewing positions of three fast ion D_α (FIDA) [13, 14, 15] systems are also indicated in the figure. The ability of FIDA systems to probe across the energetic ion distribution makes them a vital addition to confinement experiments. Radial profiles of energetic ion density are obtained from analysis of FIDA density [16] measurements. FIDA density is calculated by integrating FIDA signals over a particular energy range and then dividing out the neutral particle density due to injection from the viewed neutral beam source. This provides a method by which to compare theoretical energetic ion profiles with measurements, which would otherwise be difficult given that FIDA diagnostics measure a subset of the total energetic ion distribution.

A poloidal cross section displaying the position of relevant diagnostics is shown in figure 2. This figure contains the magnetic equilibrium from discharge 141195, which is the focus of sawtooth transport discussion in section 3. The equilibria of other discharges vary significantly from the one shown here. Diagnostics shown in figure 2 are fixed in real space and therefore accurately represent the experimental setup of other discharges. A partially transparent blue rectangle represents the typical vertical extent of neutral beam injection. This region defines the source for the active FIDA signal and therefore indicates the practical spatial limits of the FIDA diagnostics. In experiments, however, this region is extended slightly further vertically by the neutral halo region that results from charge exchange between thermal ions and the injected beam neutrals. Vertical

bars within this region are the viewing lines of the vertical FIDA system that is used to measure energetic ion density profiles for the Alfvén eigenmode (Section 4) and microturbulence studies (Section 5).

3. Transport by Sawtooth Crashes

Redistribution of the energetic ion population due to sawtooth crashes was originally observed in JET [17] and TFTR [18]. Recently, the effect has been quantified by both collective Thomson scattering [19] and FIDA [5] diagnostics on TEXTOR and DIII-D, respectively. Energetic ion density in the core is observed to decrease up to 50% in these cases. The DIII-D work incorporates a FIDA Imaging (FIDAI) system, which is a two-dimensional imaging diagnostic that provides observations across a wide poloidal cross-section as indicated by the beam footprint in figure 2. By removing the dependence of the beam injected neutral density profile, the FIDAI signal from this diagnostic (figure 6 of Ref. [5]) can be presented as a FIDA density that is proportional to the energetic ion density.

Repeatable sawteeth, in terms of amplitude and time between crashes, provide great diagnostic benefit by allowing FIDAI measurements to be collected over multiple crashes. A composite result is then constructed to represent the ensemble behavior. The central electron temperature from discharge 141195 is shown in figure 3. This temperature is measured by the electron cyclotron emission diagnostic [20] on a channel corresponding to the magnetic axis. Panel 3(a) demonstrates the nearly two seconds (from $t \approx 2 - 4$ s) of highly repeatable sawteeth. A narrow time view is shown in figure 3(b) along with vertical bars indicating the sampling width of the FIDAI system before and after a typical sawtooth crash.

Figure 4(a) displays representative electron density profiles for time periods before (solid black trace) a sawtooth crash and after (dashed blue trace). Plasma density is the parameter that most directly influences the injected neutral density profiles. These density profiles are determined by averaging data from the DIII-D Thomson scattering system [21] over the time regions indicated by vertical bars in figure 3(b). The displayed radial profiles are the result of a spline fit to these data, and the error bars are calculated through a Monte Carlo process that iterates individual spline fits based on uncertainty in the measurements. The relative change in the electron density profile before and

after the sawtooth crash is known with greater confidence than the absolute profile shape. Two individual Thomson systems measure positions in the core (typically inside of $\rho = 0.4$) and across the rest of the profile. Each system employs its own calibrations, and uncertainties in these values have the potential to exaggerate quickly evolving profile features. Based on this aspect of the measurement it is valid to consider that the electron density profile flattens due to the sawtooth perturbation, but it is not necessarily the case that a significant density hole develops. In any event, the modest change in electron density cannot account for the large change in FIDA density at the sawtooth crash as shown in figure 4(b). With a sawtooth period of approximately 100 ms, a short time window of 10 ms (the viewed beam pulse length) is chosen for time averaging FIDA measurements during periods preceding and following crashes. The two-dimensional FIDA data in figure 4(b) is spatially averaged over an approximately 5 cm tall region centered on the peak signal, which is on the midplane.

In order to quantify the redistribution of energetic ions due to the sawtooth crash, the FIDA density profiles are described by Gaussian fits that are plotted as dashed or solid red traces in figure 4(b). Properties of these fits are given in table 1. From the results shown in table 1 it is clear that the sawtooth crash widens the energetic ion profile without causing a shift. The after-crash profile is 65% wider than the before-crash profile as quantified by the full width at half-maximum.

Combining multiple FIDA diagnostics, each with a unique sampling of the energetic ion distribution, provides the ability to study sawtooth redistribution as a function of orbit type. The original FIDA diagnostic employs vertical views of the neutral beam as shown in figure 2 and features a greater sensitivity to trapped ions than passing ions. A new, tangentially viewing, FIDA diagnostic exhibits greater sensitivity to passing ions. It has been theoretically proposed [22] that orbit type determines sawtooth transport due to the extent to which the orbit is closely tied to a single flux surface. Comparisons between transport measured by separate FIDA systems in the same discharge are in qualitative agreement with the theoretical prediction that passing

particles should experience a larger transport effect than trapped particles in these discharges. Transport dependencies related to sawtooth type and ion distribution along with theoretical comparisons are the subject of a separate work following Muscatello, *et al.* [23].

4. Transport by Alfvén Eigenmodes

In reversed shear plasmas with many small amplitude ($\delta B/B \approx 2 \times 10^{-4}$) toroidal and reversed-shear Alfvén eigenmodes, the central energetic ion profile flattens. These discharges also display neutron emission levels that fall well below the classically expected values calculated by TRANSP [24] based on measured plasma profiles. Initial modeling with ORBIT [25] failed to reproduce the experimental results [26, 27] but new calculations that utilize hundreds of harmonics and include the inductive electric field predict diffusive energetic ion transport at the observed level [9, 10].

ORBIT simulations are performed using neutral beam ion deposition profiles from the NUBEAM [28, 29] module of TRANSP. ORBIT then follows the energetic ions as they interact with Alfvén eigenmodes. The mode structures and amplitudes are measured in the experiments and provided as input parameters to ORBIT, which is able to simulate the resulting energetic ion density profile. In this calculation each followed energetic ion is treated as a test particle that does not perturb the background fields or equilibrium. The total number of simulated particles is chosen to achieve appropriate resolution of the resulting transport. Details of this methodology are found in [10]. Figure 5 displays experimentally measured and theoretically determined energetic ion density profiles for discharge 122117 (a reversed shear equilibrium that is detailed in [26, 30, 31]). These profiles are determined from energetic ion pressure profiles and the approximation of constant energetic ion temperature across the plasma radius. Due to the non-uniform sampling of the energetic ion distribution by the FIDA diagnostic, that data is normalized to the equilibrium determined pressure profile as described in [26]. A classically expected profile as calculated by TRANSP is shown as the solid black trace and it exhibits a centrally peaked shape as may be expected in a case of good energetic ion confinement. Two independent measurements are shown and these exhibit a broadened profile compared to the classical expectation. The experimental profile determined from equilibrium (calculated as the difference between the total pressure from EFIT [32] equilibria constrained by motional Stark effect measurements [33] and

the measured thermal pressure) is plotted as the dotted red trace. Data points from the FIDA measurement are plotted as the solid red triangles. Both of these experimental profiles agree with the theoretical result obtained from ORBIT, which is plotted as the dashed blue trace. It is important to note that this theoretical result is a first-principles calculation using experimentally determined Alfvén eigenmode amplitudes and spatial structures. No mode adjustment, such as increasing the amplitude as attempted in [26], is performed in order to produce the broadened profile.

Modeling and simulations such as those leading to figure 5 serve to improve our understanding of Alfvén eigenmode-induced transport in the core, but it remains to link these effects with losses observed at the vessel walls [34, 35]. A newly commissioned fast ion loss detector (FILD) [36] at DIII-D observes fluctuations in ion flux that are coherent at frequencies in the TAE/RSAE range (60 – 100 kHz) [37]. The FILD consists of a scintillator surface that emits light due to energetic ion impacts. The detector is installed at a position approximately 45° below the outer midplane as shown in figure 2. This light is imaged by a camera for a two-dimensional signal that represents the energy and pitch angle of the ions. A photomultiplier tube (PMT) is also focused on the scintillator surface in order to measure fast (1 MHz) signals. Figure 6(a) shows an autopower spectrum from the FILD PMT signal averaged over a time period of Alfvén eigenmode activity (510 – 540 ms) and also at a later time during which most of this activity has subsided (710 – 740 ms). Peaks in the spectrum corresponding to Alfvén eigenmode activity are observed during the earlier time within the frequency range 60 – 90 kHz. The relevant loss activity has disappeared by the later time window. The FILD camera data indicates that these losses are ions with an energy of $E_o \approx 75$ keV and pitch of $v_{\parallel}/v \approx 0.71$. It is conceptually consistent that this energy, being the full injection of the neutral beams, is capable of interacting with Alfvén eigenmodes and being lost to the wall since this is the ion energy that drives the modes initially [38]. Using this data and the known position of the FILD aperture, the orbit representing a typical lost ion is shown in figure 6(b). As expected, this orbit is capable of originating from well within

the last closed flux surface in a region where Alfvén eigenmodes are observed to exist [39]. The confined ion that is placed onto the loss orbit through interactions with Alfvén eigenmodes is also shown. The identification of the confined orbit is treated thoroughly in [40], where the evolution from confined orbit to lost orbit is largely due to a decrease of toroidal canonical momentum.

5. Transport by Microturbulence

Energetic ions are better confined than thermal particles, in part, because the large orbits of energetic ions allow them to average over microturbulence such as the ITG and TEM modes [41]. Experiments at ASDEX-U [42] and DIII-D [11, 12] featuring off-axis neutral beam injection and MHD quiescent plasmas, however, indicate differences between the measured energetic ion confinement and the predictions of neoclassical theory. Figure 7 shows a comparison between the neoclassical and experimentally observed radial profiles of the FIDA density. A synthetic diagnostic that includes neoclassical processes to simulate the expected FIDA signal based on measured and calculated plasma parameters, FIDASIM [43], is used to generate the theoretical results for these observations.

Figure 7(a) is taken from a discharge featuring an injected neutral beam power of $P_{inj} = 3.1$ MW in which the ratio of thermal ion temperature to energetic ion energy, T_i/E , is everywhere below 0.11. Due to the thermalization process and the physics of neutral beam injection, there are ions of many energies simultaneously present in the plasma. Ranges for the ratio of T_i/E are provided using the peak ion temperature and a range of injected energies as a standardization representing the largest possibly encountered value in the experiment. In figure 7(a), the theoretical profile (solid red trace) is the same in magnitude although more peaked than the experimentally measured profile (black trace). This similarity contrasts with the situation present in panel figure 7(b), where $P_{inj} = 7.2$ MW and T_i/E increases to a maximum value of 0.38. Figure 7(b) indicates that the experimentally measured profiles are considerably smaller and flatter than the expected profile. The vertical range is the same for each panel, illustrating that the energetic ion densities have increased with increasing neutral beam injection power.

Recent theoretical and simulation work [44, 45, 46] shows that energetic ions of neutral beam injection energy in DIII-D are susceptible to microturbulence-induced transport. The transport enhancement due to microturbulence for beam ions is

theoretically expected to scale with T_i/E . Based on this collection of theory and simulation results, an experiment was designed to maximize the value of T_i/E by reducing the injection energy of the DIII-D neutral beams.

Figure 8 displays FIDA spectra for a beam injection energy of 81 keV (left column) and for 58 keV (right column). Spectral radiance, as shown in this context, is a proxy for the energetic ion density. Values of spectral radiance that fall below theoretical expectations indicate that the energetic ion density is less than expected from neoclassical theory. The discharge of reduced beam energy (right panels) features lower than expected energetic ion densities for the lowest measured vertical ion energies, E_λ [47]. This result contrasts with the full energy discharge (left panels) for which profiles at both positions largely agree with theory to within experimental uncertainty. In both discharges, data is analyzed after the plasma current flattop but before the onset of sawteeth. The spectral radiance is plotted as a function of vertical ion energy and the actual observed photon wavelength. Error bars for the experimental results are set by the standard deviation of the data ensemble collected over the 240 ms time period of interest. An additional systematic uncertainty is present due to calibration issues and may contribute a variation of up to 25% in spectral radiance amplitude. Calibration factors are an input to the simulation (FIDASIM), however, so this uncertainty does not affect conclusions concerning comparisons such as those shown in figure 8. The region of largest difference between theory and experiment occurs for $E_\lambda = 20 - 40$ keV, indicating that the effect is more pronounced for ions of lower perpendicular energy, which also feature smaller gyroradii.

This transport effect is modeled using TGYRO/TGLF [48, 49] to investigate the theoretically expected trend of increased energetic ion transport for larger values of T_i/E . Measured plasma profiles from the reduced neutral beam injection energy discharge, 138392, are provided as inputs to TGYRO/TGLF. The trace level energetic ion population is described by a Maxwellian with effective temperature, E_{EI} , varied in proportion to the fixed electron temperature ($T_e \approx T_i$). A series of calculations

are performed for different values of E_{EI} and the resulting profiles of the energetic ion diffusivity due to ITG and TEM turbulence, $D_{EI}^{ITG/TEM}$, are shown in figure 9. It is evident that as the energy of ions decreases, the turbulent particle diffusivity increases. Furthermore, the effect is more pronounced near the core, which supports the previous observations of reduced energetic ion density in the DIII-D studies. Future work will incorporate a slowing down distribution that better represents ions from neutral beam injection. Existing work comparing these different distributions finds that trends as a function of ion energy are consistent in both descriptions [50].

6. Conclusion

A wide array of energetic ion transport studies are performed at DIII-D. These experiments observe transport effects due to sawtooth crashes, Alfvén eigenmodes, and microturbulence. During sawtooth crashes, a significant reduction in the core energetic ion density is observed. A two-dimensional FIDAI system measures energetic ion redistribution after the crash and indicates that profiles widen by up to 65%. In ITER, such a large redistribution of fusion alphas in the core implies a dramatic performance reduction. Present work in this area involves quantifying the difference in sawtooth response between the passing and trapped energetic ion populations. Given the potentially complex phase space dependency of this interaction it remains a challenge to develop an accurate model that can predict the effect of sawtooth crashes on reactor performance.

Alfvén eigenmodes such as TAEs contribute to energetic ion transport even in cases where the mode amplitude is very small, $\delta B/B \approx 2 \times 10^{-4}$. Ion losses due to Alfvén eigenmodes are observed reaching detectors along the walls of multiple tokamaks [34, 35, 51]. A new procedure for modeling these coherent losses is being developed using the results of ORBIT, which simulates interactions between Alfvén waves and ions. ORBIT follows ions to the separatrix, and then an orbit calculation code tracks these particles to determine whether they strike the wall. Time dependence is taken into account and allows for modeling of losses due directly to a given mode [40].

There is growing evidence that the long wavelength components of ITG and TEM microturbulence significantly contribute to the transport of energetic ions. Recent experiments [11, 12, 42] observe enhanced levels of energetic ion transport in MHD quiescent plasmas. This turbulent transport is predicted to increase with plasma temperature and also as the energetic ion population thermalizes. The consequence for ITER operation is that fusion alphas ($T_i/E \ll 1$) should experience little to no transport enhancement and that alpha ash ($T_i/E \approx 1$) will be affected and therefore more easily lost from the plasma. Improvements to diagnostic techniques will allow for

experimental feedback to the growing collection of theory work concerning fusion alpha and alpha ash transport in the ITER regime [44, 50, 52, 53].

Continuing investigation of this turbulent transport will require improvements in both the ability to measure the effect in experiments and the ability to model it in simulations. In large-scale simulations the Gyrokinetic Toroidal Code (GTC) [54] is being used to simulate both the microturbulence and the energetic ion response taking experimentally measured plasma profiles as input parameters. This aspect of the project uses measured plasma profiles from DIII-D discharges. Values for the energetic ion diffusivity obtained from GTC simulations will be provided to TRANSP, which will then calculate the resulting energetic ion profiles for comparison with experimental measurements.

A steadily improving ability to measure and model energetic ion transport is emerging as ITER approaches. Transport due to sawtooth crashes is routinely measured and qualitatively compared to theory [23]. Quantitative simulations of this phenomena are underway and it should be expected that additional theoretical treatments will be proposed as more data becomes available. Alfvén eigenmode induced transport is quantitatively understood in cases where the mode amplitudes and spatial profiles are measured and provided to simulations. A more complete theoretical comprehension of this process must involve both the wall losses generated by the modes and the energetic ion drive of the modes themselves. Finally, a depth of theoretical results are in qualitative agreement with measurements that suggest microturbulence contributes to the transport of energetic ions and may be responsible for anomalous neutral beam current drive behavior. Improved measurements and advanced gyrokinetic simulations will improve the rigor of quantitative comparisons.

Acknowledgments

This work was supported by the US Department of Energy under SC-G903402, DE-FC02-04ER54698, DE-FG02-89ER53296, DE-FG02-08ER54999, DE-AC05-00OR22725, DE-AC02-09CH11466, DE-FG03-08ER54984, DE-FG02-07ER54917, and SciDAC GSEP. Informative discussions with Z. Lin are gratefully acknowledged. The authors would like to thank the DIII-D team for their efforts in support of the multiple experiments and diagnostic developments necessary to undertake this research. In addition, the author DCP would like to thank R.S. Granetz, the Alcator C-Mod team, and the MIT Plasma Science and Fusion Center for their hospitality during the completion of this work.

References

- [1] ITER Physics Expert Group on Energetic Particles, Heating, Current Drive, and ITER Physics Basis Editors 1999 *Nucl. Fusion* **39** 2471
- [2] Fasoli A., Gormenzano C., Berk H.L., Breizman B., Briguglio S., Darrow D.S., Gorelenkov N., Heidbrink W.W., Jaun A., Konovalov S.V., Nazikian R., Noterdaeme J.-M., Sharapov S., Shinohara K., Testa D., Tobita K., Todo Y., Vlad G., and Zonca F. 2007 *Nucl. Fusion* **47** S264
- [3] Luxon J.L. 2002 *Nucl. Fusion* **42** 614
- [4] Strait E.J. 2009 *Nucl. Fusion* **49** 104008
- [5] Van Zeeland M.A., Yu J.H., Heidbrink W.W., Brooks N.H., Burrell K.H., Chu M.S., Hyatt A.W., Muscatello C., Nazikian R., Pablant N.A., Pace D.C., Solomon W.M., and Wade M.R. 2010 *Nucl. Fusion* **50** 084002
- [6] Cheng C.Z., Chen Liu, and Chance M.S. 1985 *Ann. Physics* **161** 21–47
- [7] Cheng C.Z. and Chance M.S. 1986 *Phys. Fluids* **29** 3695–3701
- [8] Sharapov S.E., Alper B., Berk H.L., Borba D.N., Breizman B.N., Challis C.D., Fasoli A., Hawkes N.C., Hender T.C., Mailloux J., Pinches S.D., and Testa D., EFDA-JET work programme 2002 *Phys. Plasmas* **9** 2027–2036
- [9] White R.B., Gorelenkov N., Heidbrink W.W., and Van Zeeland M.A. 2010 *Plasma Phys. Control. Fusion* **52** 045012
- [10] White R.B., Gorelenkov N., Heidbrink W.W., and Van Zeeland M.A. 2010 *Phys. Plasmas* **17** 056107
- [11] Heidbrink W.W., Park J.M., Murakami M., Petty C.C., Holcomb C., and Van Zeeland M.A. 2009 *Phys. Rev. Lett.* **103** 175001
- [12] Heidbrink W.W., Murakami M., Park J.M., Petty C.C., Van Zeeland M.A., Yu J.H., and McKee G.R. 2009 *Plasma Phys. Control. Fusion* **51** 125001
- [13] Heidbrink W.W., Luo Y., Muscatello C.M., Zhu Y., and Burrell K.H. 2008 *Rev. Sci. Instrum.* **79** 10E520
- [14] Muscatello C.M., Heidbrink W.W., Taussig D., and Burrell K.H. 2010 *Rev. Sci. Instrum.* **81** 10D316
- [15] Van Zeeland M.A., Heidbrink W.W., and Yu J.H. 2009 *Plasma Phys. Control. Fusion* **51** 055001
- [16] Heidbrink W.W., Burrell K.H., Luo Y., Pablant N.A., and Ruskov E. 2004 *Plasma Phys. Control. Fusion* **46** 1855
- [17] Sadler G.J., Jarvis O.N., van Belle P., Hone M.A., Conroy S.W., Adams J.M., 1990 *Fusion Tech.* **18** 556
- [18] Fisher R.K., McChesney J.M., Parks P.B., Duong H.H., Medley S.S., Roquemore A.L., Mansfield D.K., Budny R.V., Petrov M.P., and Olson R.E. 1995 *Phys. Rev. Lett.* **75** 846–849
- [19] Nielsen S.K., Bindslev H., Salewski M., Brger A., Delabie E., Furtula V., Kantor M., Korsholm S.B., Leipold F., Meo F., Michelsen P.K., Moseev D., Oosterbeek J.W., Stejner M., Westerhof E., Woskov P., and the TEXTOR Team 2010 *Plasma Phys. Control. Fusion* **52** 092001
- [20] Austin M.E. and Lohr J. 2003 *Rev. Sci. Instrum.* **74** 1457–1459
- [21] Ponce-Marquez D.M., Bray B.D., Deterly T.M., Liu C., and Eldon D. 2010 *Rev. Sci. Instrum.* **81** 10D525
- [22] Kolesnichenko Ya.I. and Yakovenko Yu.V. 1996 *Nucl. Fusion* **36** 159
- [23] Muscatello C.M. 2009 “Fast ion transport due to the sawtooth collapse in the DIII-D tokamak,” in *Proc. of the 11th IAEA Technical Meeting on Energetic Particles in Magnetic Confinement Systems* Kyiv, Ukraine, Paper P36, <http://www.kinr.kiev.ua/TCM/index.html>
- [24] See <http://w3.pppl.gov/transp>, the official homepage of TRANSP, for information concerning the models and methods employed, in addition to usage documentation.
- [25] White R.B. and Chance M.S. 1984 *Phys. Fluids* **27** 2455–2467
- [26] Heidbrink W.W., Gorelenkov N.N., Luo Y., Van Zeeland M.A., White R.B., Austin M.E., Burrell

- K.H., Kramer G.J., Makowski M.A., McKee G.R., and Nazikian R. 2007 *Phys. Rev. Lett.* **99** 245002
- [27] Heidbrink W.W., Van Zeeland M.A., Austin M.E., Burrell K.H., Gorelenkov N.N., Kramer G.J., Luo Y., Makowski M.A., McKee G.R., Muscatello C., Nazikian R., Ruskov E., Solomon W.M., White R.B., and Zhu Y. 2008 *Nucl. Fusion* **48** 084001, 2008.
- [28] Goldston R.J., McCune D.C., Towner H.H., Davis S.L., Hawryluk R.J., and Schmidt G.L. 1981 *J. Comp. Phys.* **43** 61–78
- [29] Pankin Alexei, McCune Douglas, Andre Robert, Bateman Glenn, and Kritz Arnold 2004 *Comp. Phys. Comm.* **159** 157–184
- [30] Van Zeeland M.A., Austin M.E., Gorelenkov N.N., Heidbrink W.W., Kramer G.J., Makowski M.A., McKee G.R., Nazikia R., Ruskov E., and Turnbull A.D. 2007 *Phys. Plasmas* **14** 056102
- [31] Van Zeeland M.A., Kramer G.J., Austin M.E., Boivin R.L., Heidbrink W.W., Makowski M.A., McKee G.R., Nazikian R., Solomon W.M., and Wang G. 2006 *Phys. Rev. Lett.* **97** 135001
- [32] Lao L.L., St. John H., Stambaugh R.D., Kellman A.G., and Pfeiffer W. 1985 *Nucl. Fusion* **25** 1611
- [33] Holcomb C.T., Makowski M.A., Jayakumar R.J., Allen S.L., Ellis R.M., Geer R., Behne D., Morris K.L., Seppala L.G., and Moller J.M. 2006 *Rev. Sci. Instrum.* **77** 10E506
- [34] Duong H.H., Heidbrink W.W., Strait E.J., Petrie T.W., Lee R., Moyer R.A., and Watkins J.G. 1993 *Nucl. Fusion* **33** 749
- [35] García-Muñoz M., Fahrbach H.-U., Günter S., Igochine V., Mantsinen M.J., Maraschek M., Martin P., Piovesan P., Sassenberg K., and Zohm H. 2008 *Phys. Rev. Lett.* **100** 055005
- [36] Fisher R.K., Pace D.C., García-Muñoz M., Heidbrink W.W., Muscatello C.M., Van Zeeland M.A., and Zhu Y.B. 2010 *Rev. Sci. Instrum.* **81** 10D307
- [37] Pace D.C., Fisher R.K., García-Muñoz M., Heidbrink W.W., and Van Zeeland M.A. 2010 “Neutral beam ion losses due to Alfvén eigenmode activity in the DIII-D tokamak,” submitted to *Plasma Phys. Control. Fusion*
- [38] Nazikian R., Gorelenkov N.N., Alper B., Berk H.L., Borba D., Budny R.V., Fu G.Y., Heidbrink W.W., Kramer G.J., Makowski M.A., Pinches S.D., Sharapov S.E., Solomon W.M., Strait E.J., White R.B., Van Zeeland M.A., and JET-EFDA Contributors 2008 *Phys. Plasmas* **15** 056107
- [39] Tobias B., Classen I.G.J., Domier C.W., Heidbrink W.W., Luhmann Jr N.C., Nazikian R., Park H.K., Spong D., and Van Zeeland M.A. 2010 “Fast Ion Induced Shearing of 2D Alfvén Eigenmodes Measured by Electron Cyclotron Emission Imaging,” submitted to *Phys. Rev. Lett.*
- [40] Van Zeeland M.A., Heidbrink W.W., Fisher R.K., García-Muñoz M., Kramer G., Pace D.C., White R.B., Aekaslopolo S., Austin M.E., Boom J., Classen I., da Graça S., Geiger B., Gorelenkova M., Gorelenkov N.N., Hyatt A.W., Luhmann N., Maraschek M., McKee G.R., Muscatello C.M., Nazikian R., Park H., Sharapov S., Suttrop W., Tardini G., Tobias B.J., and Zhu Y.B., “Measurements and modeling of Alfvén eigenmode induced fast ion transport and loss in DIII-D and ASDEX Upgrade,” submitted to *Phys. Plasmas*
- [41] Mynick H.E. and Krommes John A. 1980 *Phys. Fluids* **23** 1229–1237
- [42] Günter S., Conway G., daGraça S., Fahrbach H.U., Forest C., García-Muñoz M., Hauff T., Hobirk J., Igochine V., Jenko F., Lackner K., Lauber P., McCarthy P., Maraschek M., Martin, Poli E., Sassenberg K., Strumberger E., Tardini G., Wolfrum E., Zohm H., and ASDEX Upgrade Team 2007 *Nucl. Fusion* **47** 920
- [43] Heidbrink W.W., Liu D., Luo Y., Ruskov E., and Geiger B. 2010 submitted to *Comm. Comp. Physics*
- [44] Estrada-Mila C., Candy J., and Waltz R.E. 2006 *Phys. Plasmas* **13** 112303
- [45] Zhang Wenlu, Lin Zhihong, and Chen Liu 2008 *Phys. Rev. Lett.* **101** 095001
- [46] Hauff T., Pueschel M.J., Dannert T., and Jenko F. 2009 *Phys. Rev. Lett.* **102** 075004
- [47] Heidbrink W.W., Luo Y., Burrell K.H., Harvey R.W., Pinsker R.I., and Ruskov E. 2007 *Plasma Phys. Control. Fusion* **49** 1457
- [48] Candy J., Holland C., Waltz R.E., Fahey M.R., and Belli E. 2009 *Phys. Plasmas* **16** 060704

- [49] Kinsey J.E., Staebler G.M., and Waltz R.E. 2008 *Phys. Plasmas* **15** 055908
- [50] Angioni C. and Peeters A.G. 2008 *Phys. Plasmas* **15** 052307
- [51] Darrow D.S., Fredrickson E.D., Gorelenkov N.N., Roquemore A.L., and Shinohara K. 2008 *Nucl. Fusion* **48** 084004
- [52] Albergante M., Graves J.P., Fasoli A., Jenko F., and Dannert T. 2009 *Phys. Plasmas* **16** 112301
- [53] Estrada-Mila C., Candy J., and Waltz R.E. 2005 *Phys. Plasmas* **12** 022305
- [54] Lin Z., Hahm T.S., Lee W.W., Tang W.M., and White R.B. 1998 *Science* **281** 1835–1837

Table 1. Properties of Gaussian shapes describing the FIDA density profiles before and after a sawtooth crash.

| Property | Before | After |
|--------------------------------|--------|-------|
| Center position (m) | 1.65 | 1.64 |
| Full width at half-maximum (m) | 0.37 | 0.61 |
| Reduced χ^2 | 2.20 | 0.60 |

LIST OF FIGURE CAPTIONS

Figure 1. Schematic top view of DIII-D displaying the neutral beam layout. The injection geometries of all eight neutral beams (which originate from the low-field side) are shown with respect to the standard toroidal magnetic field, B_T , and plasma current, I_p , directions. The angles listed for each beam indicate their toroidal position. Beams depicted by solid (dashed) lines are commonly referred to as tangential (perpendicular) sources. Three FIDA systems are highlighted according to which neutral beam is viewed.

Figure 2. Magnetic equilibrium in shot 141195 at $t = 2289$ ms indicating the positions of multiple diagnostics in the poloidal plane. The approximate neutral beam injection footprint is shown as the partially transparent blue rectangle. Vertical FIDA views are displayed as the yellow lines within the footprint. The fast ion loss detector (FIL) appears as the small green rectangle at approximately $[R, z] = [2.2, -0.7]$ m.

Figure 3. Central electron temperature in shot 141195. (a) Full shot length (b) narrow time region. Both traces have been smoothed for display.

Figure 4. Discharge 141195: (a) Radial electron density profiles ($\rho =$ normalized square root of the toroidal magnetic flux) representative of a time period before (solid black trace) and after (dashed blue trace) a sawtooth crash. (b) FIDA density, n_{EI} , corresponding to the time periods before and after a sawtooth crash. Gaussian fits to these profiles are shown as the dashed (After) and solid (Before) red traces.

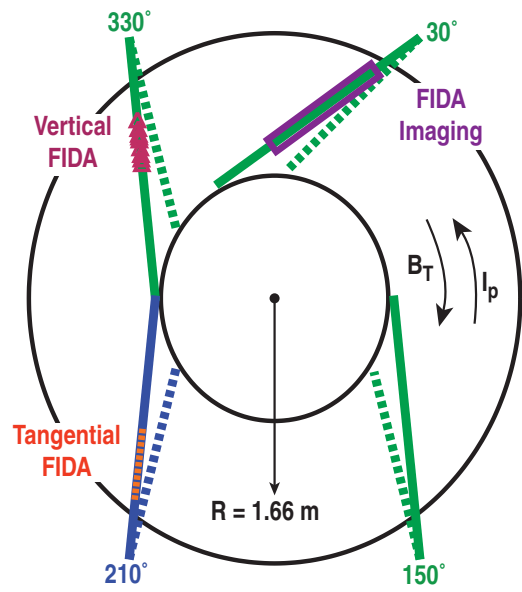
Figure 5. Energetic ion density as a function of the normalized square-root of the poloidal flux $\sqrt{\psi_p}$, for DIII-D discharge 122117. Experimental results are shown for both the FIDA density (red triangles), and from a determination of the energetic ion pressure based on magnetic equilibrium results (dotted red trace). Theoretical results from ORBIT (dashed blue trace) include transport induced by Alfvén eigenmodes. The reference profile (solid black trace) is obtained from a classical model in TRANSP that does not include transport due to Alfvén eigenmodes. This data is compiled between [10] and [26].

Figure 6. Energetic ion loss results from DIII-D discharge 142111. (a) Autopower spectrum from the FILD PMT signal averaged over $510 \leq t \leq 540$ ms (solid black) and $710 \leq t \leq 740$ ms (dotted red). (b) Trajectory of a confined ion orbit (blue trace) that leads to the observed loss orbit (red trace). The loss orbit is reconstructed based on FILD camera data at $t = 570$ ms and a region corresponding to the FILD position is indicated by the labeled square. Ion orbit properties are: $E_o = 75$ keV, $v_{\parallel}/v = 0.707$ (45° pitch angle).

Figure 7. Radial profile of proportional energetic ion density (FIDA density) as calculated based on neoclassical, collision-dominated theory (solid red trace) and from experimental measurements (black data points). The FIDA data is integrated over the vertical energy range of 20 – 60 keV. (a) Discharge 133981 with $P_{inj} = 3.1$ MW and FIDA data averaged over $2000 \leq t \leq 3000$ ms encompassing the range $0.02 \leq T_i/E \leq 0.11$. (b) Discharge 134426 with $P_{inj} = 7.2$ MW and FIDA data averaged over $2000 \leq t \leq 3000$ ms encompassing the range $0.13 \leq T_i/E \leq 0.38$.

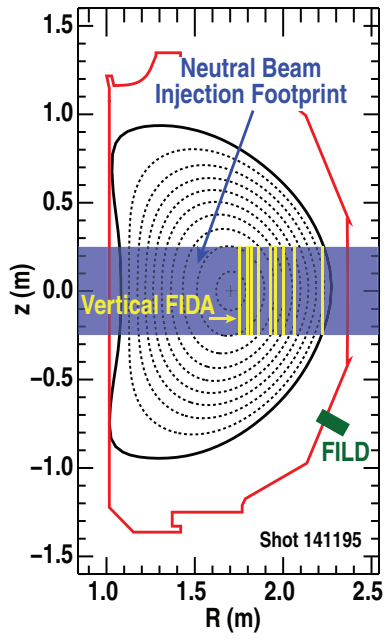
Figure 8. Comparison between measured FIDA spectra (solid black traces) and simulated spectra (dashed red traces, using FIDASIM v2). (Left) Shot 138385, $E_{inj} = 81$ keV, $P_{inj} = 4.8$ MW. (Right) Shot 138392, $E_{inj} = 58$ keV, $P_{inj} = 4.9$ MW. (a) $\rho = 0.13$, (b) $\rho = 0.15$, (c) $\rho = 0.36$, (d) $\rho = 0.38$.

Figure 9. Radial profile of the energetic ion diffusivity due to ITG and TEM turbulence, $D_{EI}^{ITG/TEM}$, normalized to the thermal ion energy diffusivity, χ_i , as calculated using TGYRO/TGLF for shot 138392.



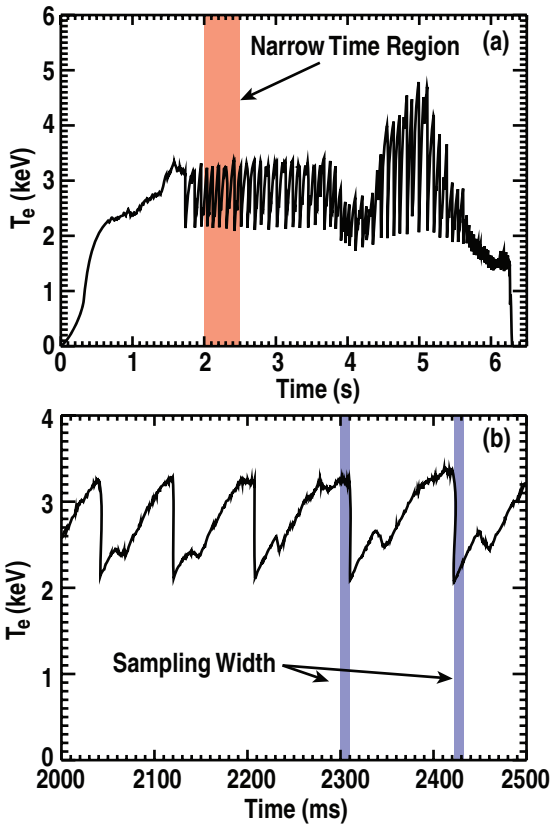
D.C. Pace

Figure 1



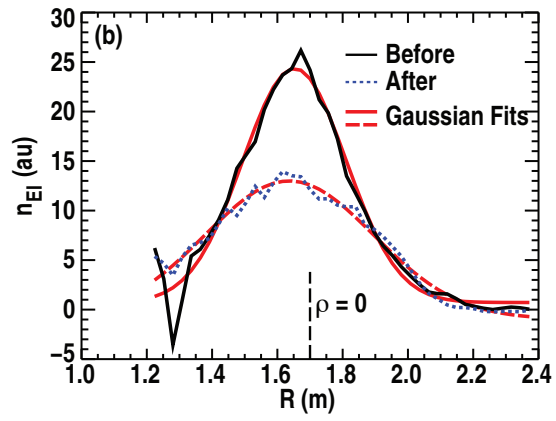
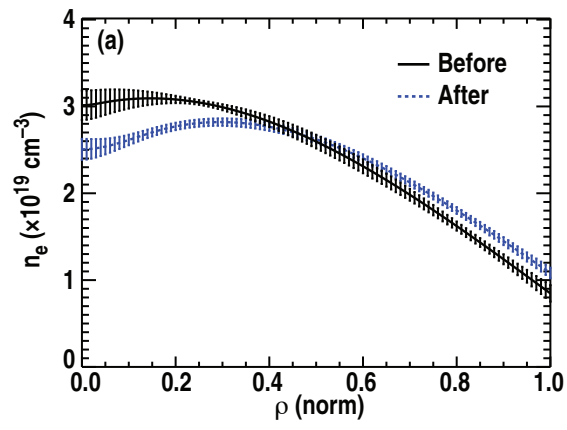
D.C. Pace

Figure 2



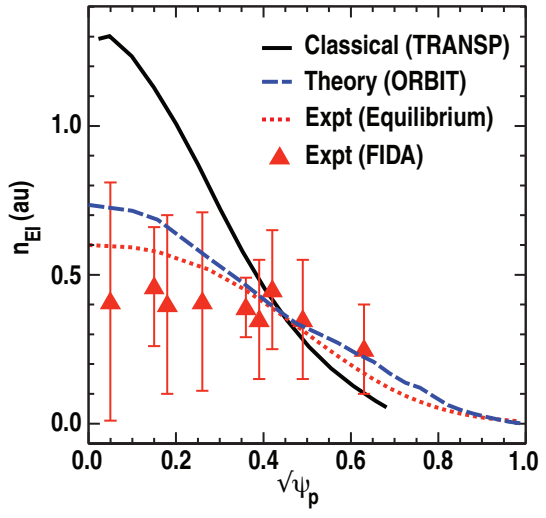
D.C. Pace

Figure 3



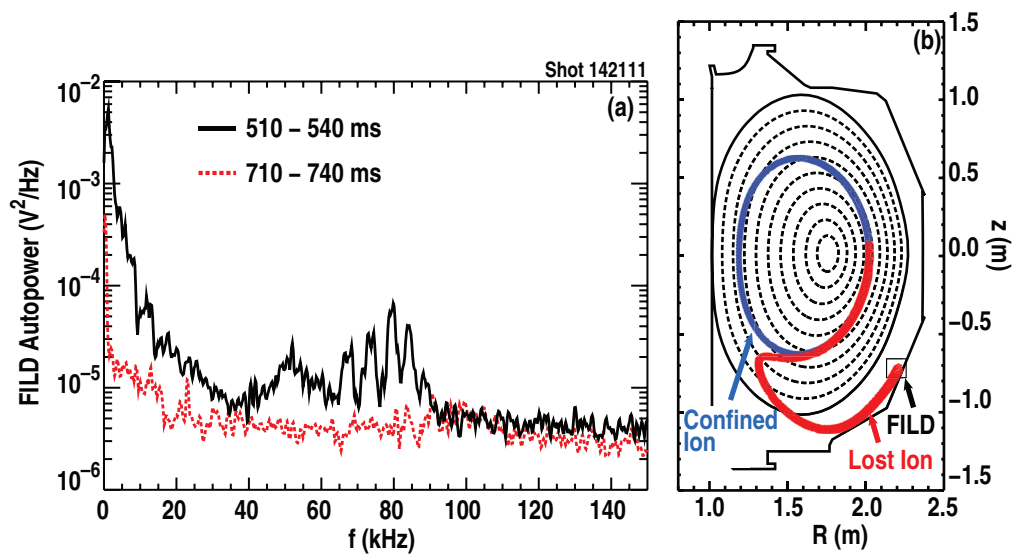
D.C. Pace

Figure 4



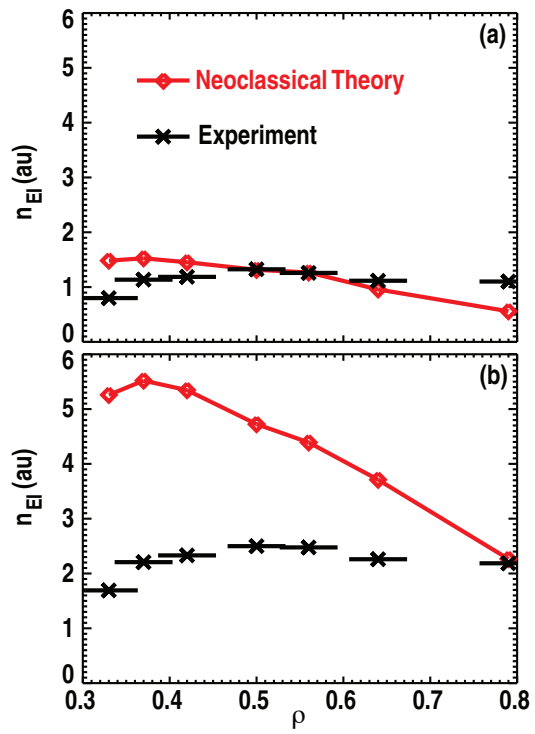
D.C. Pace

Figure 5



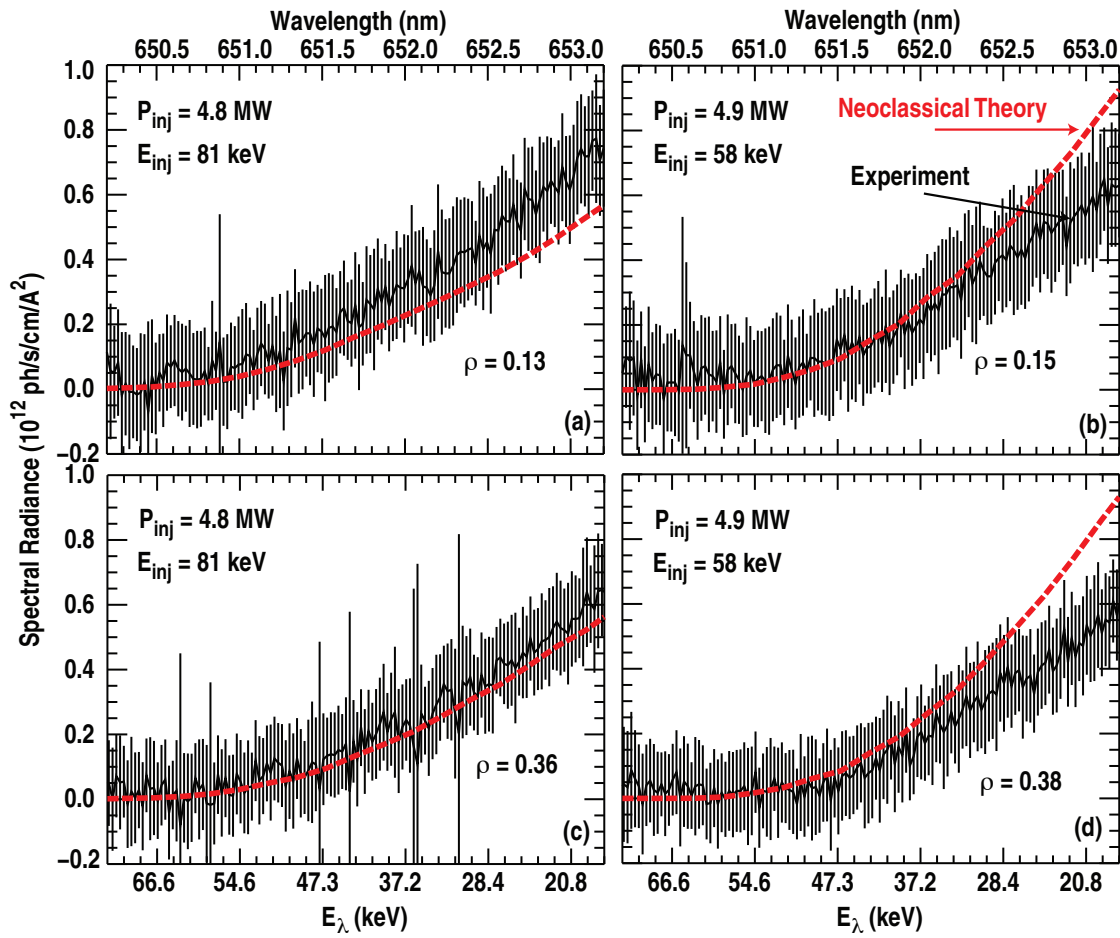
D.C. Pace

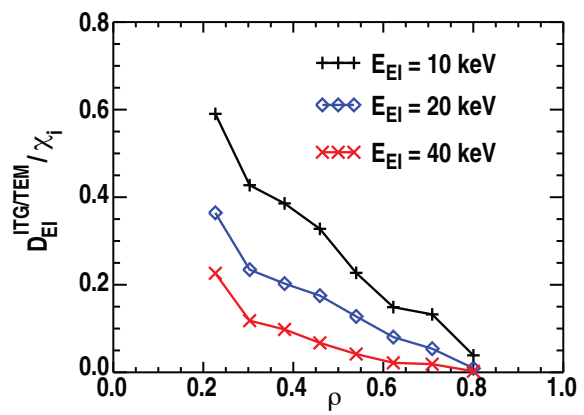
Figure 6



D.C. Pace

Figure 7





D.C. Pace

Figure 9